Symmetry-breaking orbital anisotropy observed for detwinned $Ba(Fe_{1-x}Co_x)_2As_2$ above the spin density wave transition

Ming Yi[a,b], Donghui Lu[c], Jiun-Haw Chu[a,b], James G. Analytis[a,b], Adam P. Sorini[a], Alexander F. Kemper[a], Brian Moritz[a], Sung-Kwan Mo[d], Rob G. Moore[a], Makoto Hashimoto[a,b,d], Wei-Sheng Lee[a], Zahid Hussain[d], Thomas P. Devereaux[a,b], Ian R. Fisher[a,b], and Zhi-Xun Shen[a,b,1]

[a]Stanford Institute for Materials and Energy Sciences, SLAC National Accelerator Laboratory, 2575 Sand Hill Road, Menlo Park, CA 94025; [b]Geballe Laboratory for Advanced Materials, Departments of Physics and Applied Physics, Stanford University, Stanford, CA 94305; [c]Stanford Synchrotron Radiation Lightsource, SLAC National Accelerator Laboratory, 2575 Sand Hill Road, Menlo Park, CA 94025; and [d]Advanced Light Source, Lawrence Berkeley National Laboratory, Berkeley, CA 94720

Edited* by Laura H. Greene, University of Illinois at Urbana-Champaign, Urbana, IL, and approved March 8, 2011 (received for review October 24, 2010)

Nematicity, defined as broken rotational symmetry, has recently been observed in competing phases proximate to the superconducting phase in the cuprate high-temperature superconductors. Similarly, the new iron-based high-temperature superconductors exhibit a tetragonal-to-orthorhombic structural transition (i.e., a broken C_4 symmetry) that either precedes or is coincident with a collinear spin density wave (SDW) transition in undoped parent compounds, and superconductivity arises when both transitions are suppressed via doping. Evidence for strong in-plane anisotropy in the SDW state in this family of compounds has been reported by neutron scattering, scanning tunneling microscopy, and transport measurements. Here, we present an angle-resolved photoemission spectroscopy study of detwinned single crystals of a representative family of electron-doped iron-arsenide superconductors, $Ba(Fe_{1-x}Co_x)_2As_2$ in the underdoped region. The crystals were detwinned via application of in-plane uniaxial stress, enabling measurements of single domain electronic structure in the orthorhombic state. At low temperatures, our results clearly demonstrate an in-plane electronic anisotropy characterized by a large energy splitting of two orthogonal bands with dominant d_{xz} and d_{yz} character, which is consistent with anisotropy observed by other probes. For compositions $x > 0$, for which the structural transition (T_S) precedes the magnetic transition (T_{SDW}), an anisotropic splitting is observed to develop above T_{SDW}, indicating that it is specifically associated with T_S. For unstressed crystals, the band splitting is observed close to T_S, whereas for stressed crystals, the splitting is observed to considerably higher temperatures, revealing the presence of a surprisingly large in-plane nematic susceptibility in the electronic structure.

Correlated electron systems owe their emergent phenomena to a complex array of competing electronic phases. Among these, a nematic phase is one where rotational symmetry is spontaneously broken without breaking translational symmetry (1, 2). Two well-established examples are found in certain quantum Hall states (3) and in the bilayer ruthenate $Sr_3Ru_2O_7$ (4), both of which exhibit a large transport anisotropy under the application of large magnetic fields, even though they seem to originate from apparently different physics. Recently, evidence of nematicity has also been reported in the pseudogap phase of cuprate high-temperature (high-T_C) superconductors, in both $YBa_2Cu_3O_y$ (5) and $Bi_2Sr_2CaCu_2O_{8+\delta}$ (6). The proximity of the pseudogap phase to superconductivity raises the question of what role nematicity plays in relation to the mechanism of high-T_C superconductivity. Intriguingly, the newly discovered iron pnictide high-T_C superconductors also exhibit a nematic phase in the form of a tetragonal-to-orthorhombic structural transition that either precedes or accompanies the onset of long-range antiferromagnetic order (7, 8), both of which are suppressed with doping leading to superconductivity (9–11). Evidences of in-plane anisotropy have been reported by neutron scattering (12), scanning tunneling microscopy (13), and transport measurements (14–16). The physical origin of the structural transition has been discussed in terms of both spin fluctuations (17–21) and also orbital order (22–28). Here, we present results of an angle-resolved photoemission spectroscopy (ARPES) study of underdoped $Ba(Fe_{1-x}Co_x)_2As_2$ that reveal an energy splitting of bands with principle d_{xz} and d_{yz} character that we show is associated with the structural transition. Although the splitting can be anticipated purely on symmetry grounds, the large magnitude (approximately 80 meV at 10 K for the parent compound) provides a quantitative test for theories of nematic order in this family of compounds. Moreover, we find that application of uniaxial stress causes the onset of the band splitting to occur well above the structural transition (T_S), indicating the presence of a large Ising nematic susceptibility.

In the orthorhombic phase, $Ba(Fe_{1-x}Co_x)_2As_2$ tends to form dense structural twins (29) which can easily obscure in-plane anisotropy. If the domains are large compared to the beam size, then information about the in-plane electronic anisotropy can be obtained by ARPES (30). Here, we apply an in-plane uniaxial stress to detwin the single crystals that we study, and hence avoid the problems of domain mixing, enabling us to study the effect of uniaxial stress on the electronic structure *above* T_S.

Results

In Fig. 1, we compare the Fermi surfaces (FSs) of twinned and detwinned $BaFe_2As_2$ ($T_S = T_{SDW} = 138$ K) crystals in the spin density wave (SDW) state measured under the same experimental conditions. Here, we use the Brillouin zone (BZ) notations corresponding to the true crystallographic 2-Fe unit cell in which Γ-X is along the antiferromagnetic crystal axis and Γ-Y is along the ferromagnetic (FM) crystal axis (Fig. 1 *A*–*C*). In the twinned case (Fig. 1*D*), the nearly orthogonal domains mix signals from both Γ-X and Γ-Y directions, masking out any possible intrinsic differences between these directions and leading to complex FS topology and band dispersions. However, once detwinned, one clearly observes that the electronic structure along Γ-X (Fig. 1*E*)

Author contributions: M.Y. and D.L. designed research; M.Y., D.L., and W.-S.L. performed research; A.P.S., A.F.K., and B.M. performed calculations; J.-H.C. and J.G.A. provided samples; S.-K.M., R.G.M., and M.H. provided instrumental support; M.Y. and D.L. analyzed data; Z.H., T.P.D., I.R.F., and Z.-X.S. advised; and M.Y., D.L., T.P.D., I.R.F., and Z.-X.S. wrote the paper.

The authors declare no conflict of interest.

*This Direct Submission article had a prearranged editor.

Freely available online through the PNAS open access option.

[1]To whom correspondence may be addressed at: Geballe Laboratory for Advanced Materials, McCullough Building 342 476 Lomita Mall Stanford, CA 94305-4045 E-mail: zxshen@stanford.edu.

This article contains supporting information online at www.pnas.org/lookup/suppl/doi:10.1073/pnas.1015572108/-/DCSupplemental.

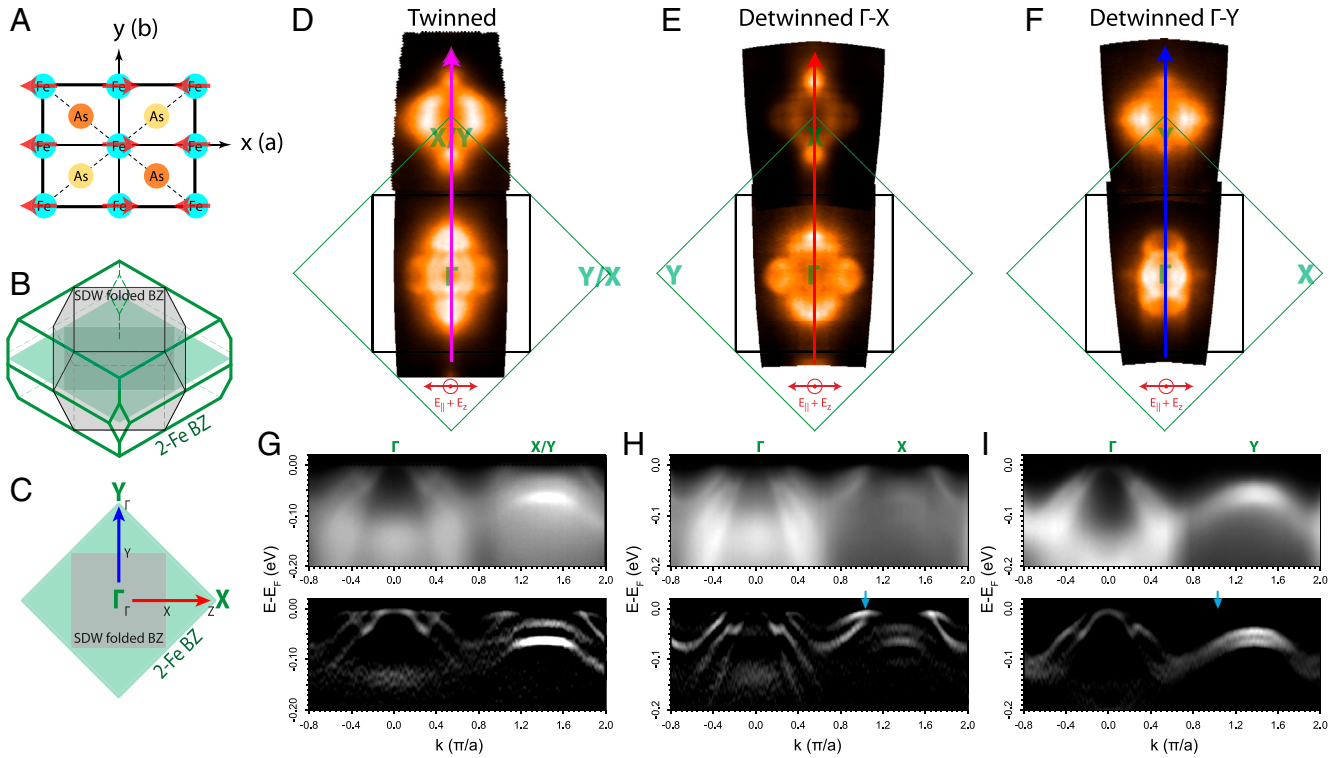

Fig. 1. Anisotropy of electronic structure observed on detwinned $BaFe_2As_2$. (*A*) Schematic of unit cell of $BaFe_2As_2$ in the orthorhombic SDW state where spins are FM along the shorter *b* axis and antiferromagnetic (AFM) along the longer *a* axis. (*B*) Schematic of 3D BZ for the body-centered tetragonal PM state (green) and base-centered orthorhombic SDW state (black). Projected 2D BZs are shown as shaded planes. (*C*) Notations shown on 2D projection of respective BZ. We use notations pertaining to the PM BZ (green) throughout, where Γ-*X* is along the AFM direction, and Γ-*Y* is along the FM direction. (*D*) FS in the SDW state measured on twinned crystals in which the *X* and *Y* points are mixed and indistinguishable due to existence of twin domains. (*E* and *F*) FS in the SDW state measured on detwinned crystal along Γ-*X* and Γ-*Y*, respectively, showing strong anisotropy along these two directions. (*G–I*) Corresponding spectral images along high-symmetry lines (*Upper*) and their second derivatives (*Lower*) for the FSs shown above demonstrating the anisotropy in the band dispersions. All data were measured at 10 K, with 25 eV photons, and polarization vectors labeled in red. All FSs presented in the paper are made with an integration window of 5 meV about E_F.

and Γ-*Y* (Fig. 1*F*) directions are different. Moreover, the anisotropy of the FS is further reinforced by the band dispersions measured along these two high-symmetry directions (Fig. 1 *H* and *I*), where the strong anisotropy of the band structure is not limited to near the Fermi level (E_F).

Next, we study the FS topology under different photon polarizations to reveal the underlying band character (Fig. 2 *A–C*). For a multiorbital system, variation of the orbital character around the FS can result in differed intensity patterns for different polarizations due to photoemission matrix element effects (*SI Text*). The dramatic variation in intensity of the domain-resolved FS under different polarizations indicates that the FS of $BaFe_2As_2$ retains its strong multiorbital character even in the SDW state, contrary to the claims of a recent laser-ARPES report on twinned crystals (31). Taking the FS pieces highlighted under different polarizations together, we arrive at the complete FS in the reconstructed SDW BZ (Fig. 2*D*), consisting of two hole pockets (α, β) and an electron pocket (γ) centered on Γ, surrounded by two bright spots (δ) along Γ-*X* and two bigger petal pockets (ε) along Γ-*Y*. A detailed k_z-dependence study on detwinned crystals shows that the qualitative anisotropy between k_x and k_y is robust for all k_z values (see *SI Text*). As shown in Fig. 2*A*, the FS topology around the *Y* point is similar to the *X* point, as expected under BZ folding after SDW reconstruction. However, C_4 (fourfold) rotational symmetry is broken, that is, the Γ-*X* and Γ-*Y* *directions*, which should be equivalent under C_4 rotational symmetry, are no longer the same. To ensure that this effect is not due to extrinsic photoemission matrix elements, we chose a polarization whose symmetry is equivalent for both Γ-*X* and Γ-*Y* directions, and yet still observe the same anisotropy (Fig. 2*C*). Hence, the observed difference unambiguously demonstrates that the *x–y* directional anisotropy reflects the intrinsic property of the electronic structure in the SDW state.

The most anisotropic features on the FS are the bright spots along Γ-*X* and petals along Γ-*Y*. As seen from band dispersions (Fig. 2 *E* and *F*), these features are results of anticrossing between hole and electron bands. Moreover, the bands cross at different energies in the two directions: close to E_F along Γ-*X*, inducing tiny Fermi pockets observed as bright spots (Fig. 2*E*), and 30 meV below E_F along Γ-*Y* (Fig. 2*F*) resulting in bigger electron pockets on the FS. These small Fermi pockets [0.2% and 1.4% of the paramagnetic (PM) BZ] are in good agreement with quantum oscillation reports (32). We note that such band crossings were discussed in early five-band model calculations where they were linked to Dirac cone features (33, 34). The bright spots and petal-like FSs have been observed in earlier ARPES data on twinned $BaFe_2As_2$ (35–37) and $SrFe_2As_2$ (38). However, detwinned crystals here allow us to experimentally observe that the bright spots and petals reside along two orthogonal directions, manifesting the broken C_4 rotational symmetry of the electronic structure in the orthorhombic collinear SDW state.

To trace the origin of the anisotropy, we performed a temperature-dependence study (Fig. 3*A*). The most anisotropic feature in the low-temperature state is a pronounced hole-like dispersion near the *X* and *Y* points, which as shown evolves from the same hole-like dispersion in the PM state. Now, considering the fact that polarization perpendicular to each high-symmetry cut was used in Fig. 3*A*, only those bands with orbital character odd with respect to each cut direction can be observed. Hence for cuts along Γ-*X*, only bands of d_{yz} and d_{xy} orbitals can be observed;

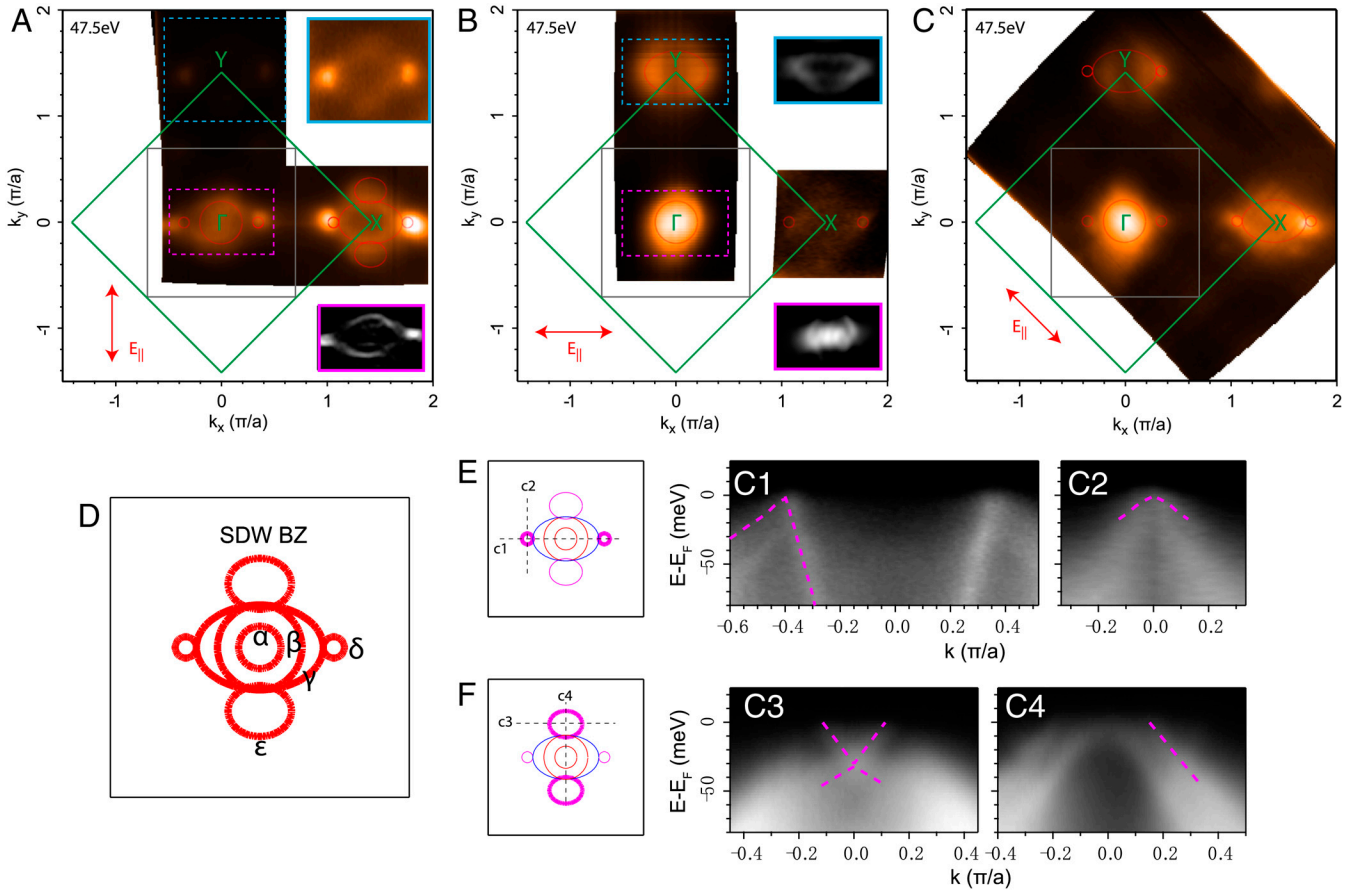

Fig. 2. Multiorbital SDW FSs of $BaFe_2As_2$ probed by different polarizations. (*A–C*) FSs probed with different polarizations, indicated by red arrows. Insets (cyan and magenta) show corresponding dotted regions for better contrast. Intensity enhancement of the *Y* region (cyan inset in *A*) reveals similar FS topology as *X* region with C_4 rotational symmetry broken. All other insets are second derivatives of the corresponding FSs. Different parts of the FS are enhanced or suppressed under different polarizations, indicating multiorbital character of the FS in the SDW state. Outline of FS visible under each polarization is overlaid on measured FS in the corresponding panels. (*D*) A summary of measured FS outlines in the reconstructed SDW BZ. (*E*) Spectral image cuts through the bright spots along Γ-*X* showing band crossing near E_F. Cuts taken near the *Y* point in the experimental setup of *A*. (*F*) Spectral image cuts through the petal along Γ-*Y* showing similar band crossing further below E_F. Cuts taken near the Γ point in the experimental setup of Fig. 1*E* (C3) and Fig. 1*F* (C4). Electron dispersion is suppressed along the high-symmetry cut in C4 due to photoemission matrix elements for this geometry.

whereas for cuts along Γ-*Y*, only d_{xz} and d_{xy} orbitals can be seen. Moreover, d_{xy} has very little intensity in the first BZ, whereas d_{yz} and d_{xz} are much stronger in the corresponding geometries (see *SI Text*). Therefore, the prominent hole-like dispersion that we observe on these particular cuts must be d_{yz} along Γ-*X* and d_{xz} along Γ-*Y*, consistent with orbital assignments by local-density approximation calculations (39).

Having identified the orbital characters of this anisotropic feature, we make the observation that for temperatures well above T_{SDW} in the PM state of $BaFe_2As_2$, the d_{yz} band along Γ-*X* and the d_{xz} band along Γ-*Y* are degenerate in energy, which is symmetric under the exchange of *x* and *y* axes, reflecting an inherent C_4 rotationally symmetric electronic structure as also confirmed by the measured FS (Fig. 3*B*). As temperature is lowered toward T_{SDW}, the degeneracy is lifted as the d_{yz} band along Γ-*X* shifts up and crosses E_F, whereas the d_{xz} band along Γ-*Y* shifts down, which are no longer equivalent under the exchange of *x* and *y* axes. This anisotropic band shift results in an unequal occupation of the d_{yz} and d_{xz} orbitals. The splitting between the originally degenerate d_{yz} and d_{xz} bands reaches approximately 60 meV at 80 K ($T_{SDW} = 138$ K) (Fig. 3*A*). Even more interestingly, a careful look at the detailed temperature evolution reveals that the anisotropic band shift persists above T_{SDW}, consistent with resistivity measurements reporting anisotropy developing above T_{SDW} even for undoped compound held under uniaxial stress (15, 16).

To further study this phenomenon, we measured underdoped compound $Ba(Fe_{0.975}Co_{0.025})_2As_2$ detwinned by uniaxial stress, for which T_S (99 K) and T_{SDW} (94.5 K) are split. First, for this doping, we observe similar anisotropy in the electronic structure as that of the undoped parent compound (see *SI Text*). More importantly, the temperature-dependence study (Fig. 3*C*) reveals that the anisotropic shift of the d_{yz} and d_{xz} bands is clearly present well above the long-range magnetic ordering temperature, and for a temperature window even bigger than that of the undoped parent compound, consistent with transport results (15). To quantitatively illustrate the band shift with temperature, we plot the energy positions of the d_{yz} and d_{xz} bands at the same representative momentum position along the Γ-*X* and Γ-*Y* high-symmetry lines (for analysis details, see *SI Text*), revealing a trend that is reminiscent of the anisotropy observed above T_{SDW} in bulk sensitive resistivity measurements (Fig. 3*E*). Hence, our ARPES study here reveals that the intriguing anisotropy seen in the resistivity is associated with a large C_4 symmetry-breaking modification of the electronic structure that develops almost fully above the long-range magnetic order.

To gauge the effect of the uniaxial stress, we also measured unstressed twinned samples for comparison, for which the energy separation between the d_{yz} and d_{xz} bands can be measured as they appear on the same cut due to twin domain mixing (Fig. 3*D*). We observe that below T_{SDW} the splitting in the unstressed sample has the same magnitude within experimental uncertainty as that

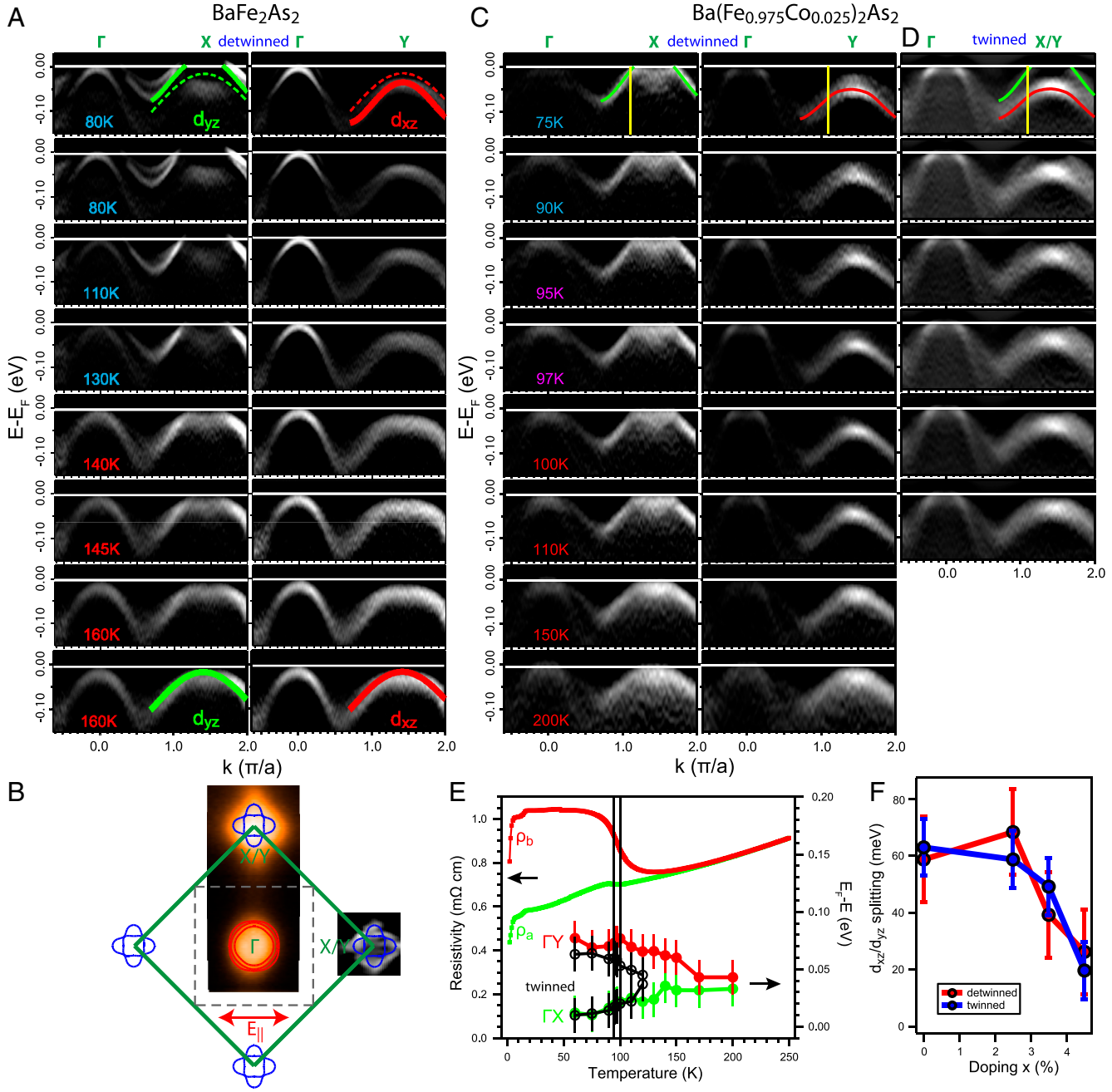

Fig. 3. Temperature and doping dependence: Anisotropic band shift observed above T_{SDW} on detwinned $Ba(Fe_{1-x}Co_x)_2As_2$. (*A*) Temperature dependence of anisotropic band dispersion (second derivative) along Γ-*X* and Γ-*Y* high-symmetry lines taken on $BaFe_2As_2$ through T_S/T_{SDW} (138 K), with 47.5 eV photons ($k_z = 0$). Γ-*X* (Γ-*Y*) cuts were measured under polarization setup of Fig. 2*A* (Fig. 2*B*). Along Γ-*X*, only d_{yz} orbital is highlighted by photoemission matrix elements on the high-symmetry cut, whereas the same is true for d_{xz} orbital along Γ-*Y*. Band guides to the eye are drawn to indicate the shift with temperature. Dotted lines are bands from the PM state for comparison. (*B*) FS of $BaFe_2As_2$ taken above T_S/T_{SDW} confirming C_4 symmetry, with 54 eV photons ($k_z = \pi/2$). The image shown at the *X*/*Y* point to the right of Γ is the second derivative of corresponding FS at the *X*/*Y* point to the top of Γ for better contrast. (*C*) Temperature dependence of the anisotropic band dispersion between Γ-*X* and Γ-*Y* (second derivatives) on $Ba(Fe_{0.975}Co_{0.025})_2As_2$ through T_{SDW} (94.5 K), with 62 eV photons ($k_z = \pi$). (*D*) Same measurements on unstressed twinned sample for comparison. (*E*) Energy position of hole dispersions near *X* (green) and *Y* (red) relative to E_F at the representative momentum marked by yellow lines in *C* plotted as a function of temperature, measured on both detwinned and unstressed crystals, compared with resistivity measurements reproduced from ref. 15. (*F*) Doping dependence of the d_{xz}/d_{yz} band splitting measured at momentum $k = 0.9\pi/a$ taken at 10 K, with 47.5 eV photons ($k_z = 0$).

found for the stressed crystals. However, whereas the splitting in the stressed samples persists well above T_S, it decreases rapidly starting around T_{SDW} and diminishes slightly above T_S for the unstressed samples (Fig. 3*E*). That is, for an unstressed crystal, the electronic structure respects C_4 symmetry well above T_S. Approaching T_S, rotational symmetry is broken as an anisotropic band shift rapidly develops between the d_{yz} and d_{xz} orbitals, leading to a symmetry broken electronic structure in the orthorhombic state (Fig. 4). In the case of a stressed crystal, the extended temperature window above T_S in which anisotropy persists can be understood as arising from the small uniaxial stress in the sample, which acts as a symmetry-breaking field for the structural phase transition, smearing out T_S into a cross-over temperature while leaving T_{SDW} well defined and little affected with increasing

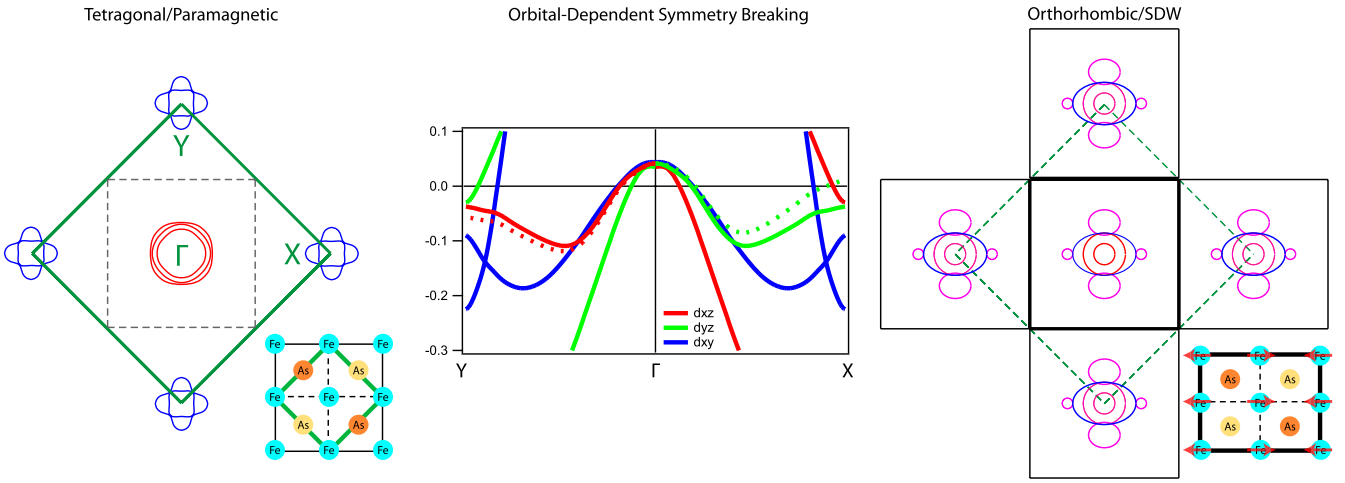

Fig. 4. Schematic of development of anisotropy in electronic structure of underdoped $Ba(Fe_{1-x}Co_x)_2As_2$. In the tetragonal PM state (*Left*), both lattice and spin have C_4 rotational symmetry which is reflected in the observed C_4 symmetric electronic structure. C_4 rotational symmetry is also preserved in the orbital content as d_{xz} band along Γ-*Y* and d_{yz} band along Γ-*X* are degenerate (solid lines in center). As the system approaches T_{SDW}, C_4 rotational symmetry in orbital degree of freedom is broken as the d_{xz} band shifts down and d_{yz} band shifts up (dashed lines in center). The anisotropy in the band dispersions is then manifested in the lowered symmetry of the orthorhombic SDW state, as the observed FS is strongly anisotropic reflecting the C_2 rotational symmetry of the spin and lattice structure (*Right*). Red (blue) pockets indicate hole (electron) character, whereas magenta indicates pockets resulting from hybridization of electron and hole features.

pressure (15). The extended temperature window above T_{SDW} in which anisotropy persists induced by the uniaxial stress reveals a large intrinsic electronic nematic susceptibility. We note that, although a lattice distortion exists below T_S, it is too small to account for the large magnitude of the energy splitting we observe in the orthorhombic PM state, as a nonmagnetic band calculation accounting for the lattice distortion shows only a splitting of 10 meV (see *SI Text*), well below the observed value of up to 80 meV.

We also carried out a more detailed doping-dependence study of the anisotropic energy splitting between the d_{yz} and d_{xz} bands at a temperature (10 K) well below T_{SDW} on both twinned and detwinned crystals in the underdoped region (see *SI Text*), which confirms that the full magnitude of the splitting is little affected by the uniaxial stress. Moreover, the magnitude of the splitting decreases monotonically with doping (Fig. 3*F*)—a trend consistent with the suppression of the magnetic ordering temperature and structural distortion (40), as well as optical conductivity measurement on detwinned crystals showing smaller dichroism for doped samples compared to the parent compound (41). This composition dependence contrasts with transport measurements, for which the maximum in-plane resistivity anisotropy is observed not for zero doping, but dopings closer to the superconducting dome (15).

Discussion

Our findings have several important implications for theories of the electronic structure of the iron pnictides. First, we observe that a large rotational symmetry-breaking modification of the electronic structure occurs from the tetragonal PM state to the orthorhombic SDW state, providing a microscopic basis for the many signs of in-plane anisotropy reported in literature (12–16, 41). Furthermore, this broken symmetry is also revealed here to be manifested in an unbalanced occupation in the d_{yz} and d_{xz} orbitals, which develops almost fully at T_{SDW}. This observation alone does not distinguish the origin of the structural phase transition. The large amplitude of the band splitting draws attention to the possibility that the orbital degree of freedom might play an important role. In this context, it is worth noting that, although it is experimentally difficult to calculate the orbital anisotropy over the whole BZ, a simple estimate based on a modified band structure calculation incorporating experimentally observed orbital splitting shows the orbital anisotropy over the entire FS to be on the order of only 10–20% (see *SI Text*), which is too small to be associated with a simple Kugel–Khomskii type orbital ordering (42). Finally, the electronic anisotropy seen in the orbital degree of freedom is observed to onset at a temperature well above the structural transition in stressed crystals. This temperature window, which indicates the involvement of fluctuations, appears to be bigger for doping levels closer to the superconducting dome, a trend also seen in transport measurements, suggesting that fluctuation effects, possibly of orbital origin, may play an important role in high-temperature superconductivity in the iron pnictides.

Materials and Methods

High-quality single crystals of $Ba(Fe_{1-x}Co_x)_2As_2$ were grown using the self-flux method (10). Detwinned single crystals of $Ba(Fe_{1-x}Co_x)_2As_2$ were obtained using a modified version of the mechanical device reported by Chu et al. (15), where uniaxial stress was applied at room temperature and stressed crystals cooled down to measurement temperature before cleaving in situ. ARPES measurements were carried out at both beamline 5-4 of the Stanford Synchrotron Radiation Lightsource and beamline 10.0.1 of the Advanced Light Source using SCIENTA R4000 electron analyzers. The total energy resolution was set to 15 meV or better and the angular resolution was 0.3°. Single crystals were cleaved in situ at 10 K for low-temperature measurements, 80 K (60 K) for temperature-dependence measurements on undoped (doped) compound, and 150 K for high-temperature measurements. All measurements were done in ultrahigh-vacuum chambers with a base pressure lower than 4×10^{-11} torr.

We note that our detwinning method does not affect the intrinsic electronic structure of the crystal because a mixture of the FS and band dispersions along the two directions on detwinned crystal reproduces those observed on the twinned crystal, as expected under domain mixing (Fig. 1). Furthermore, the high degree of detwinning is evident in contrasting band dispersions along the two orthogonal directions. For example, the bands highlighted by the arrow along Γ-*X* (Fig. 1*H*) are almost indiscernible along Γ-*Y* on a highly detwinned sample (Fig. 1*I*), whereas for a partially detwinned crystal, faint traces of these bands would be seen along Γ-*Y* due to mixing of Γ-*X* and Γ-*Y*.

ACKNOWLEDGMENTS. The authors are grateful for helpful discussions with C.-C. Chen, R.-H. He, I. I. Mazin, Y. Ran, D. J. Singh, F. Wang, D.-H. Lee, J. P. Hu, and Z. Y. Lu. ARPES experiments were performed at the Stanford Synchrotron Radiation Lightsource and the Advanced Light Source, which are both operated by the Office of Basic Energy Science, US Department

of Energy (DOE). The Stanford work is supported by DOE Office of Basic Energy Science, Division of Materials Science and Engineering, under Contract DE-AC02-76SF00515. M.Y. thanks the National Science Foundation Graduate Research Fellowship Program for financial support.

1. Kivelson SA, Fradkin E, Emery VJ (1998) Electronic liquid-crystal phases of a doped Mott insulator. *Nature* 393:550–553.
2. Fradkin E, Kivelson SA, Lawler MJ, Eisenstein JP, Mackenzie AP (2010) Nematic Fermi fluids in condensed matter physics. *Annu Rev Condens Matt Phys* 1:153–178.
3. Lilly MP, Cooper KB, Eisenstein JP, Pfeiffer LN, West KW (1999) Evidence for an anisotropic state of two-dimensional electrons in high Landau levels. *Phys Rev Lett* 82:394–397.
4. Borzi RA, et al. (2007) Formation of a nematic fluid at high fields in $Sr_3Ru_2O_7$. *Science* 315:214–217.
5. Daou R, et al. (2010) Broken rotational symmetry in the pseudogap phase of a high-T_C superconductor. *Nature* 463:519–522.
6. Lawler MJ, et al. (2010) Intra-unit-cell electronic nematicity of the high-T_C copper-oxide pseudogap states. *Nature* 466:347–351.
7. de la Cruz C, et al. (2008) Magnetic order versus superconductivity in the iron-based layered $La(O_{1-x}F_x)FeAs$ systems. *Nature* 453:899–902.
8. Huang Q, et al. (2008) Neutron-diffraction measurements of magnetic order and a structural transition in the parent $BaFe_2As_2$ compound of FeAs-based high-temperature superconductors. *Phys Rev Lett* 101:257003.
9. Rotter M, Tegel M, Johrendt D (2008) Superconductivity at 38 K in the iron arsenide $(Ba_{1-x}K_x)Fe_2As_2$. *Phys Rev Lett* 101:107006.
10. Chu J-H, et al. (2009) Determination of the phase diagram of the electron-doped superconductor $Ba(Fe_{1-x}Co_x)_2As_2$. *Phys Rev B* 79:014506.
11. Ni N, et al. (2008) Effects of Co substitution on thermodynamic and transport properties and anisotropic H_{c2} in $Ba(Fe_{1-x}Co_x)_2As_2$ single crystals. *Phys Rev B* 78:214515.
12. Zhao J, et al. (2009) Spin waves and magnetic exchange interactions in $CaFe_2As_2$. *Nat Phys* 5:555–560.
13. Chuang T-M, et al. (2010) Nematic electronic structure in the "parent" state of the iron-based superconductor $Ca(Fe_{1-x}Co_x)_2As_2$. *Science* 327:181–184.
14. Chu J-H, et al. (2009) In-plane electronic anisotropy in underdoped $Ba(Fe_{1-x}Co_x)_2As_2$ revealed by partial detwinning in a magnetic field. *Phys Rev B* 81:214502.
15. Chu J-H, et al. (2010) In-plane resistivity anisotropy in an underdoped iron arsenide superconductor. *Science* 329:824–826.
16. Tanatar MA, et al. (2010) Uniaxial-strain mechanical detwinning of $CaFe_2As_2$ and $BaFe_2As_2$ crystals: Optical and transport study. *Phys Rev B* 81:184508.
17. Mazin II, Johannes MD (2009) A key role for unusual spin dynamics in ferropnictides. *Nat Phys* 5:141–145.
18. Fang C, et al. (2008) Theory of electron nematic order in LaFeAsO. *Phys Rev B* 77:224509.
19. Xu C, Muller M, Sachdev S (2008) Ising and spin orders in the iron-based superconductors. *Phys Rev B* 78:020501(R).
20. Fernandes R, et al. (2009) Effects of nematic fluctuations on the elastic properties of iron arsenide superconductors. *Phys Rev Lett* 105:157003.
21. Daghofer M, Nicholson A, Moreo A, Dagotto E (2010) Three orbital model for the iron-based superconductors. *Phys Rev B* 81:014511.
22. Lee C-C, Yin W-G, Ku W (2009) Ferro-orbital order and strong magnetic anisotropy in the parent compounds of iron-pnictide superconductors. *Phys Rev Lett* 103:267001.
23. Kruger F, Kumar S, Zaanen J, van den Brink J (2009) Spin-orbital frustrations and anomalous metallic state in iron-pnictide superconductors. *Phys Rev B* 79:054504.
24. Bascones E, Calderon MJ, Valenzuela B (2010) Low magnetization and anisotropy in the antiferromagnetic state of undoped iron pnictides. *Phys Rev Lett* 104:227201.
25. Yin ZP, Pickett WE (2010) Crystal symmetry and magnetic order in iron pnictides: A tight-binding Wannier function analysis. *Phys Rev B* 81:174534.
26. Lv W, Kruger F, Phillips P (2010) Orbital ordering and unfrustrated $(\pi,0)$ magnetism from degenerate double exchange in the pnictides. *Phys Rev B* 82:045125.
27. Chen C-C, et al. (2010) Orbital order and spontaneous orthorhombicity in iron pnictides. *Phys Rev B* 82:100504(R).
28. Laad MS, Craco L (2010) Theory of orbital nematicity in underdoped iron arsenides. arXiv:1010.2940v1.
29. Tanatar MA, et al. (2009) Direct imaging of the structural domains in the iron pnictides AFe_2As_2 (A = Ca, Sr, Ba). *Phys Rev B* 79:180508(R).
30. Wang Q, et al. (2010) Uniaxial "nematic-like" electronic structure and Fermi surface of untwinned $CaFe_2As_2$. arXiv:1009.0271v1.
31. Shimojima T, et al. (2010) Orbital-dependent modifications of electronic structure across the magnetostructural transition in $BaFe_2As_2$. *Phys Rev Lett* 104:057002.
32. Analytis JG, et al. (2009) Quantum oscillations in the parent pnictide $BaFe_2As_2$: Itinerant electrons in the reconstructed state. *Phys Rev B* 80:064507.
33. Ran Y, et al. (2009) Nodal spin density wave and band topology of the FeAs-based materials. *Phys Rev B* 79:014505.
34. Morinari T, Kaneshita E, Tohyama T (2010) Topological and transport properties of Dirac Fermions in an antiferromagnetic metallic phase of iron-based superconductors. *Phys Rev Lett* 105:037203.
35. Yi M, et al. (2009) Unconventional electronic reconstruction in undoped $(Ba,Sr)Fe_2As_2$ across the spin density wave transition. *Phys Rev B* 80:174510.
36. Richard P, et al. (2010) Observation of Dirac cone electronic dispersion in $BaFe_2As_2$. *Phys Rev Lett* 104:137001.
37. Liu C, et al. (2010) Evidence for a Lifshitz transition in electron-doped iron arsenic superconductors at the onset of superconductivity. *Nat Phys* 6:419–423.
38. Hsieh D, et al. (2008) Experimental determination of the microscopic origin of magnetism in parent iron pnictides. arXiv:0812.2289v1.
39. Graser S, et al. (2010) Spin fluctuations and superconductivity in a three-dimensional tight-binding model for $BaFe_2As_2$. *Phys Rev B* 81:214503.
40. Prozorov R, et al. (2009) Intrinsic pinning on structural domains in underdoped single crystals of $Ba(Fe_{1-x}Co_x)_2As_2$. *Phys Rev B* 80:174517.
41. Dusza A, et al. (2010) Anisotropic charge dynamics in detwinned $Ba(Fe_{1-x}Co_x)_2As_2$. arXiv:1007.2543v1.
42. Kugel KI, Khomskii DI (1982) The Jahn-Teller effect and magnetism: Transition metal compounds. *Sov Phys Uspekhi* 25:231–256.